

Article

# Improved Intrinsic Nonlinear Characteristics of Ta<sub>2</sub>O<sub>5</sub>/Al<sub>2</sub>O<sub>3</sub>-Based Resistive Random-Access Memory for High-Density Memory Applications

Ji-Ho Ryu <sup>1</sup> and Sungjun Kim <sup>2,\*</sup><sup>1</sup> Electronics Engineering, Chungbuk National University, Cheongju 28644, Korea; jhryu13@naver.com<sup>2</sup> Division of Electronics and Electrical Engineering, Dongguk University, Seoul 04620, Korea

\* Correspondence: sungjun@dongguk.edu

Received: 13 August 2020; Accepted: 17 September 2020; Published: 21 September 2020



**Abstract:** The major hindrance for high-density application of two-terminal resistive random-access memory (RRAM) array design is unintentional sneak path leakage through adjacent cells. Herein, we propose a bilayer structure of Ta<sub>2</sub>O<sub>5</sub>/Al<sub>2</sub>O<sub>3</sub>-based bipolar type RRAM by evaluating the intrinsic nonlinear characteristics without integration with an additional transistor and selector device. We conducted X-ray photoelectron spectroscopy (XPS) analysis with different etching times to verify Ta<sub>2</sub>O<sub>5</sub>/Al<sub>2</sub>O<sub>3</sub> layers deposited on the TiN bottom electrode. The optimized nonlinear properties with current suppression are obtained by varying Al<sub>2</sub>O<sub>3</sub> thickness. The maximum nonlinearity (~71) is achieved in a Ta<sub>2</sub>O<sub>5</sub>/Al<sub>2</sub>O<sub>3</sub> (3 nm) sample. Furthermore, we estimated the comparative read margin based on the I-V characteristics with different thicknesses of Al<sub>2</sub>O<sub>3</sub> film for the crossbar array applications. We expect that this study about the effect of the Al<sub>2</sub>O<sub>3</sub> tunnel barrier thickness on Ta<sub>2</sub>O<sub>5</sub>-based memristors could provide a guideline for developing a selector-less RRAM application.

**Keywords:** memristor; RRAM; nonlinearity; read margin; conduction mechanism; F–N tunneling; XPS

## 1. Introduction

The interest in developing an alternative storage device to overcome the scaling-limit issue has been extensively growing during the past two decades [1–3]. Among the potential candidates for next-generation non-volatile memory, resistive switching random-access memory (RRAM) has received significant attention in recent years due to its noticeable resistive switching characteristics, such as fast switching speed [4,5], low power consumption [6], complementary metal-oxide-semiconductor (CMOS) compatibility [7], and multifunctional applicability, which is suitable for non-volatile memory [8–10], logic in memory [11–13], and neuromorphic device applications [14–17]. The RRAM is generally composed of a simple and compact metal-insulator-metal (MIM) structure, which has a major specialty in minimizing cell size, as  $4F^2$  ( $F$  is feature size for lithography) [18,19]. Recently, several cases have been reported of fabricating a crossbar array for high integration using RRAM cells in various ways [20–22]. However, the crossbar array structure including two terminal RRAM cells has the issue about reading disturbance between adjacent cells because of the sneak current issue. [23,24]. Several approaches including one transistor-one resistor (1T-1R) [25], one diode-one resistor (1D-1R) [26], and one selector-one resistor (1S-1R) [27] have been introduced to overcome this challenging issue. However, in terms of spatial integration, the intrinsic nonlinear characteristic in RRAM is more desirable than the above candidates. Numerous studies have analyzed the effect of nonlinear switching with various material structures [28–32]. However, additional efficient methods are available to optimize and utilize the selector-less property in more detail.

In this work, we propose the built-in nonlinear characteristics in Pt/Ta<sub>2</sub>O<sub>5</sub>/Al<sub>2</sub>O<sub>3</sub>/TiN devices to realize the selector-less RRAM application. First, we confirm the comparative X-ray photoelectron

spectroscopy (XPS) analysis by etching for a top-down layer with information from the investigated material. Depending on the  $\text{Al}_2\text{O}_3$  thickness, we investigate the detailed nonlinear switching performances in both positive and negative bias to ensure high nonlinearity. The read margin from I–V characteristics of the devices with different  $\text{Al}_2\text{O}_3$  thickness is calculated using the half-bias scheme in crossbar array application. We suggest the conceptual physical mechanism in the oxide layer to explain the specific effect of  $\text{Al}_2\text{O}_3$  modulation.

## 2. Experimental Procedure

The schematic configuration of the Pt/ $\text{Ta}_2\text{O}_5$ / $\text{Al}_2\text{O}_3$ /TiN structure on the  $\text{SiO}_2$ /Si substrate is presented in Figure 1a, and the fabrication process is summarized in Figure 1b. First, we deposited the TiN as a bottom electrode (BE) on a  $\text{SiO}_2$ /Si substrate by direct current (DC) sputtering with the thickness of approximately 100 nm. Afterward, the  $\text{Al}_2\text{O}_3$  thin layer was deposited by thermal atomic layer deposition (TALD) at 350°C with different thicknesses for 1 nm, 3 nm, and 5 nm. We used trimethylaluminum (TMA) and ozone ( $\text{O}_3$ ) as a precursor for Al and O, respectively [33]. Then we deposited 15-nm-thick tantalum oxide ( $\text{Ta}_2\text{O}_5$ ) as a main switching layer on the  $\text{Al}_2\text{O}_3$  film by reactive DC sputtering from a tantalum target with Ar (8 sccm) and  $\text{O}_2$  (12 sccm) at room temperature. Finally, the 100-nm-thick Pt top electrode (TE) was deposited by e-beam evaporation and patterned through a shadow mask containing a circular pattern with a diameter of 100  $\mu\text{m}$ . We observed the cross-sectional image from the transmission electron microscopy (TEM) in Figure 1c. The electrical properties in the DC sweep and transient modes were measured using a semiconductor parameter analyzer (Keithley 4200-SCS and 4225-PMU ultrafast module, Solon, OH, USA). Transmission electron microscope (TEM) and energy-dispersive X-ray spectroscopy (EDS) was conducted by the JEOL (JEM-2100F, Tokyo, JAPAN). Moreover, we applied a voltage to the Pt TE, while the TiN BE was grounded during the DC and pulse measurement.

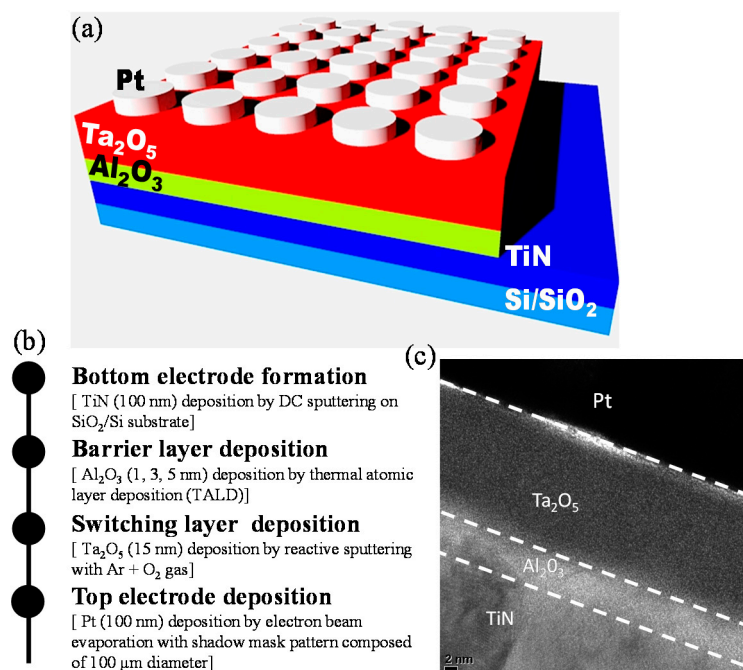


**Figure 1.** (a) Schematic illustration of Pt/ $\text{Ta}_2\text{O}_5$ / $\text{Al}_2\text{O}_3$ /TiN device; (b) flow chart of device fabrication of the device; (c) Cross-sectional transmission electron microscopy (TEM) image of the device.

## 3. Results and Discussion

In order to identify the chemical composition with a binding energy of  $\text{Ta}_2\text{O}_5$ / $\text{Al}_2\text{O}_3$ /TiN structure, we carried out the XPS analysis to verify the comparative atomic spectra by  $\text{Ar}^+$  etching from the

surface. The detailed XPS working conditions are summarized in Figure S1. Figure 1a–c shows the XPS spectra of Ta 4f, Al 2p, and Ti 2p, respectively. Ta 4f<sub>7/2</sub> and Ta 4f<sub>5/2</sub> peaks were centered at 26.3 eV and 28.2 eV, respectively, at the surface (0 s) [34]. Subsequently, the suboxide was detected after 5 s because of the Ta-O-Al bond near the Ta<sub>2</sub>O<sub>5</sub>/Al<sub>2</sub>O<sub>3</sub> interface [35]. For the Al 2p peaks shown in Figure 2b, until the etching for 10 s, the Al 2p peak was undetectable because of the bulk Ta<sub>2</sub>O<sub>5</sub> layer. The Al 2p peak was detected with 10 s after etching, indicating the Al<sup>3+</sup> state (75.8 eV) of stoichiometric Al<sub>2</sub>O<sub>3</sub> [36]. The second peak with low intensity is related to combination of Ta 4f and Al 2p. After 20 s, the sub-oxide peaks at a lower binding energy frequently appeared because of the formation of Al-O-Ti near the Al<sub>2</sub>O<sub>3</sub>/TiN interface. The Ti 2p spectra contains the dominant two doublets of Ti2p<sub>3/2</sub> (454.2 eV) and Ti2p<sub>1/2</sub> (460.15 eV) that stem from TiN in Figure 2c [37]. The other doublets at the low binding energy were affected by a reaction in the Al<sub>2</sub>O<sub>3</sub>/TiN interface, such as TiON.

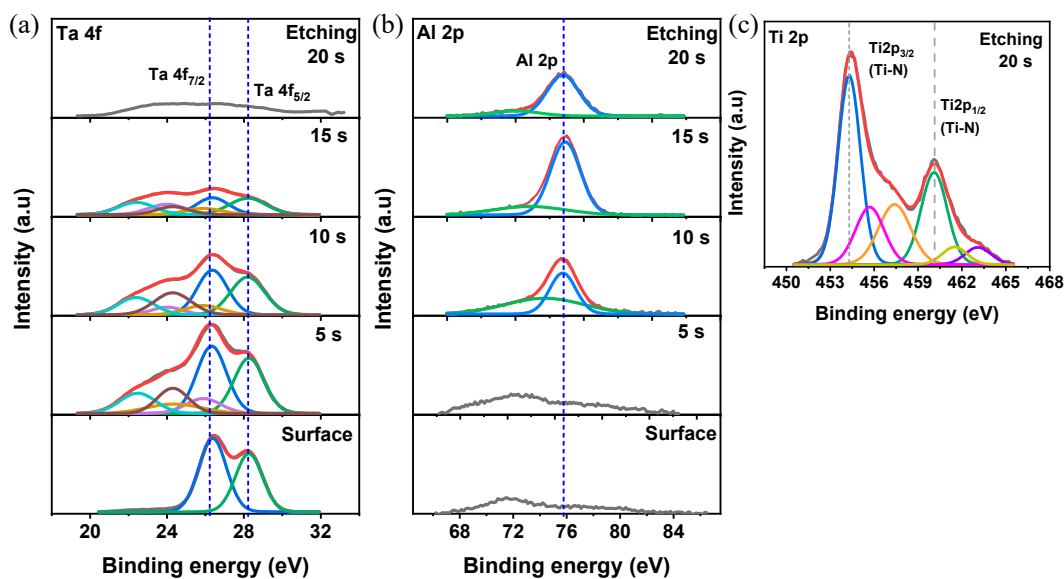


**Figure 2.** XPS analysis by Ar<sup>+</sup> etching of Ta<sub>2</sub>O<sub>5</sub>/Al<sub>2</sub>O<sub>3</sub>/TiN layer: (a) Ta 4f spectra of the Ta<sub>2</sub>O<sub>5</sub> film; (b) Al 2p spectra of the Al<sub>2</sub>O<sub>3</sub> film; (c) Ti 2p spectra of the TiN bottom electrode.

To activate the oxygen ions/vacancies for the filament formation, a one-step electroforming process was induced to make the low-resistance state (LRS) while limiting the compliance current (CC) of 1 mA, as in Figure S2. Note that the electroforming voltage increased with the thickness of the Al<sub>2</sub>O<sub>3</sub> layer. The CC was confined to 1 mA in order to prevent the device from permanent breakdown during the electroforming process. In Figure 3a–d, the experimental DC *I*–*V* characteristics of Pt/Ta<sub>2</sub>O<sub>5</sub>/TiN, Pt/Ta<sub>2</sub>O<sub>5</sub>/Al<sub>2</sub>O<sub>3</sub> (1 nm)/TiN, Pt/Ta<sub>2</sub>O<sub>5</sub>/Al<sub>2</sub>O<sub>3</sub> (3 nm)/TiN, and Pt/Ta<sub>2</sub>O<sub>5</sub>/Al<sub>2</sub>O<sub>3</sub> (5 nm)/TiN devices are investigated to verify the nonlinear tendency depending on the thickness of Al<sub>2</sub>O<sub>3</sub> layer. The results suggest that inserting an Al<sub>2</sub>O<sub>3</sub> layer from 1 nm to 3 nm reinforces the nonlinear switching characteristics during the multiple cycles. In particular, the current increases abruptly, and then decrease gradually with the voltage sweep in a positive region, indicating that it is like a complementary resistive switching (CRS) curve. Note again that the current must be suppressed at low voltage to obtain a nonlinear curve. Therefore, it is important that the Al<sub>2</sub>O<sub>3</sub> tunnel barrier should be maintained with the insulated property in the LRS (discussed in more detail later). The nonlinear property in the LRS loses for the Pt/Ta<sub>2</sub>O<sub>5</sub>/Al<sub>2</sub>O<sub>3</sub> (5 nm)/TiN device because a high forming voltage makes the current overshoot [38,39]. It should be noticed that the optimized Al<sub>2</sub>O<sub>3</sub> thickness between the Ta<sub>2</sub>O<sub>5</sub> and TiN layer is the most important factor in ensuring the nonlinear characteristics after the electroforming process.

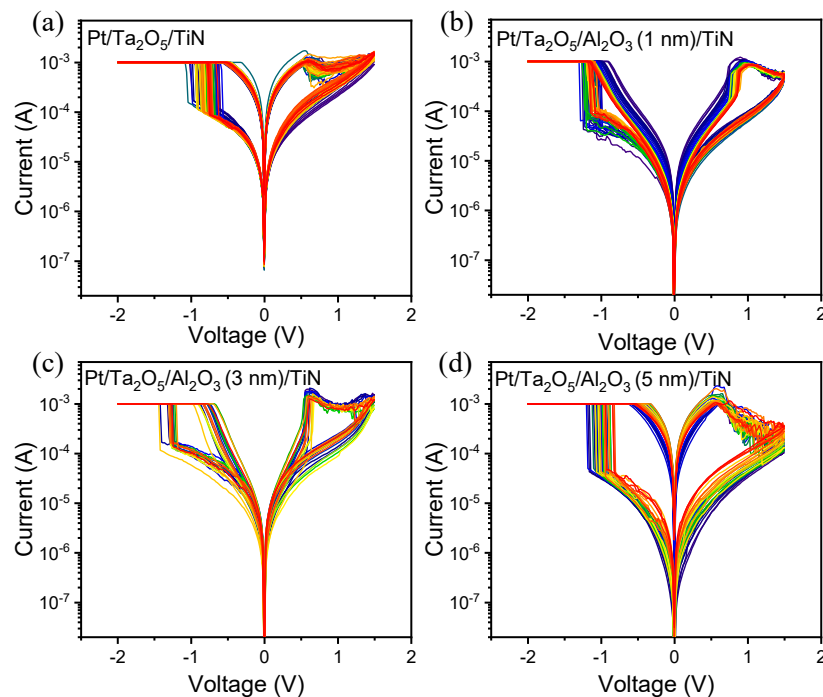


**Figure 3.** Experimental  $I$ – $V$  results of (a) Pt/Ta<sub>2</sub>O<sub>5</sub>/TiN; (b) Pt/Ta<sub>2</sub>O<sub>5</sub>/Al<sub>2</sub>O<sub>3</sub> (1 nm)/TiN; (c) Pt/Ta<sub>2</sub>O<sub>5</sub>/Al<sub>2</sub>O<sub>3</sub> (3 nm)/TiN; (d) Pt/Ta<sub>2</sub>O<sub>5</sub>/Al<sub>2</sub>O<sub>3</sub> (5 nm)/TiN devices.

To specifically analyze the nonlinear characteristics of the Pt/Ta<sub>2</sub>O<sub>5</sub>/Al<sub>2</sub>O<sub>3</sub> (3 nm)/TiN device, the SET process occurs with the CC of 1 mA by applying  $-2$  V to turn into the LRS. On the other hand, the RESET process occurs by sweeping from  $0$  V to  $1.5$  V to turn back to high resistance state (HRS). The nonlinear  $I$ – $V$  characteristics, which indicate the suppression of the current in a low-voltage region, are clearly demonstrated by the Pt/Ta<sub>2</sub>O<sub>5</sub>/Al<sub>2</sub>O<sub>3</sub> (3 nm)/TiN device structure in Figure 4a. The nonlinearity is defined as the value of the current at read voltage ( $V_{\text{read}}$ ) divided by the current at half read voltage ( $V_{1/2\text{read}}$ ). In Figure 4b, the pulse current responses are observed to demonstrate the nonlinear property of the Pt/Ta<sub>2</sub>O<sub>5</sub>/Al<sub>2</sub>O<sub>3</sub>(3 nm)/TiN device. The currents are significantly suppressed when the applied voltages are low ( $<|1$  V). Figure 4c shows the statistical distribution of the nonlinearity in both polarities for 4 devices. Especially, the maximum nonlinearity ( $\sim 71$ ) is achieved by the Pt/Ta<sub>2</sub>O<sub>5</sub>/Al<sub>2</sub>O<sub>3</sub>(3 nm)/TiN device in a positive bias. The nonlinearity can be improved by inserting an Al<sub>2</sub>O<sub>3</sub> layer with appropriate thickness in both polarities.

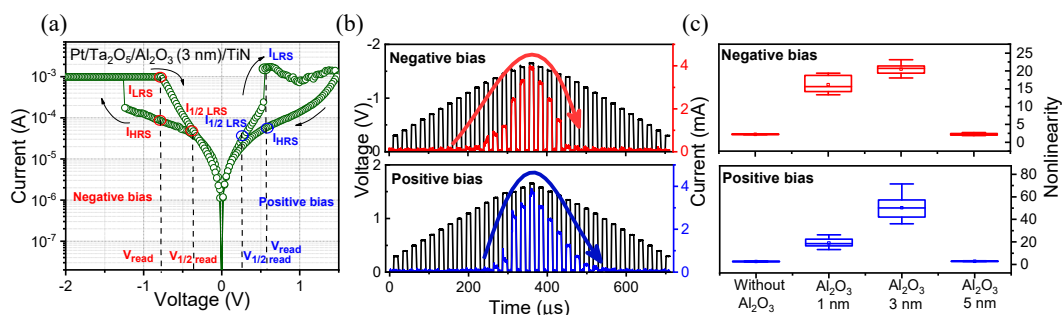


**Figure 4.** (a) Nonlinear  $I$ – $V$  curve of Pt/Ta<sub>2</sub>O<sub>5</sub>/Al<sub>2</sub>O<sub>3</sub> (3 nm)/TiN selector-less RRAM device. (b) Pulse responses of suppressed characteristics in Pt/Ta<sub>2</sub>O<sub>5</sub>/Al<sub>2</sub>O<sub>3</sub> (3 nm)/TiN device. (c) Comparison box plot of nonlinear parameter in both polarities.

The most effective use of the nonlinear characteristics in the Pt/Ta<sub>2</sub>O<sub>5</sub>/Al<sub>2</sub>O<sub>3</sub>/TiN device is the suppression of the sneak path to implement high-density crossbar arrays in Figure 5a. The RRAM cells

with high nonlinearity have a strong immunity to overcome the sneak path interference [40]. The read margin is considered to evaluate the relationship between the array density and nonlinear behaviors in detail. Note that the read margin degrades with the increasing number of word lines because of a high sneak path current through the adjacent cells with increasing array size [41]. For the calculation based on Kirchhoff's circuit law, the virtual two-terminal passive crossbar arrays ( $N$  rows  $\times$   $N$  columns) can be simplified as the equivalent circuit and calculated from the measured  $I$ - $V$  characteristics with a half-bias read scheme [42]. The detailed process of calculation for the read margin is explained in Figure S3. Figure 5b presents the read margin by a unified half-bias scheme in Pt/Ta<sub>2</sub>O<sub>5</sub>/TiN device and Pt/Ta<sub>2</sub>O<sub>5</sub>/Al<sub>2</sub>O<sub>3</sub>(1, 3, 5 nm)/TiN devices. The array size ( $N$  rows  $\times$   $N$  columns) is extracted by 10% criteria to evaluate a reliable sensing margin. Compared to the Pt/Ta<sub>2</sub>O<sub>5</sub>/TiN device and Pt/Ta<sub>2</sub>O<sub>5</sub>/Al<sub>2</sub>O<sub>3</sub>(1, 5 nm)/TiN devices, the Pt/Ta<sub>2</sub>O<sub>5</sub>/Al<sub>2</sub>O<sub>3</sub> (3 nm)/TiN device has a higher read margin (~71) because of the highest nonlinearity through optimization of the Al<sub>2</sub>O<sub>3</sub> thickness.

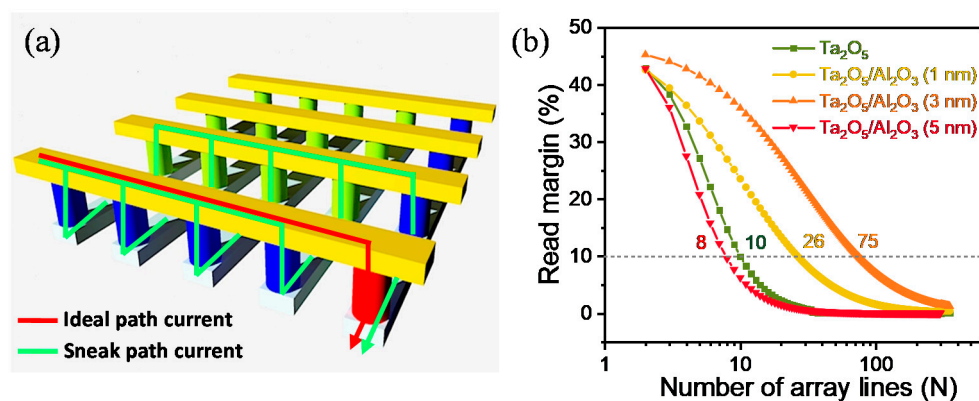


**Figure 5.** (a) Schematics of two-terminal RRAM based crossbar array configuration for high integrated application. (b) Calculated read margin as a function of number of array line for four devices.

To analyze the possible conducting mechanism process and the filamentary model of nonlinear characteristics in the Pt/Ta<sub>2</sub>O<sub>5</sub>/Al<sub>2</sub>O<sub>3</sub>/TiN device, we divided the experimental  $I$ - $V$  curve in a positive bias into 4 regions to express the movement of oxygen vacancies in oxide layers (Figure 6a). The slope in log-log fitting and the current is at a low voltage in region 1 because the Al<sub>2</sub>O<sub>3</sub> layer somewhat insulates the LRS. The Al<sub>2</sub>O<sub>3</sub> tunnel barrier layer acts as the main role in nonlinear characteristics, by suppressing the current at low voltage. When the oxygen vacancies are increased by an increased electric field (E-field), Fowler–Nordheim (F–N) tunneling, which is one of the well-known conduction mechanisms in the thin-film dielectric [43], can be the dominant conduction mechanism in Figure 6c. It is also confirmed that the  $I$ - $V$  curve in region 2 is well matched with  $\ln(I/V^2)$  vs.  $1/V$  fitting for F–N tunneling in Figure 6a [44]. When the electric field is strongly applied inside the Al<sub>2</sub>O<sub>3</sub> tunnel barrier, the barrier viewed from the metal electrode is deformed into a triangle, so that the movement of the carrier becomes easier. In other words, the effective Al<sub>2</sub>O<sub>3</sub> barrier becomes thinner. At the end of saturation with the more increased E-field, the Al<sub>2</sub>O<sub>3</sub> also has become activated to form a conducting filament with high conductivity, and the device is changed to LRS for the set process in region 3, as shown in Figure 6d. Then finally, in Figure 6e, the overinflated E-field elicits the filament breakage in Figure 6e. The temporal LRS turns into HRS for a reset transition. These experimental results are well matched with previously reported research [45–48].

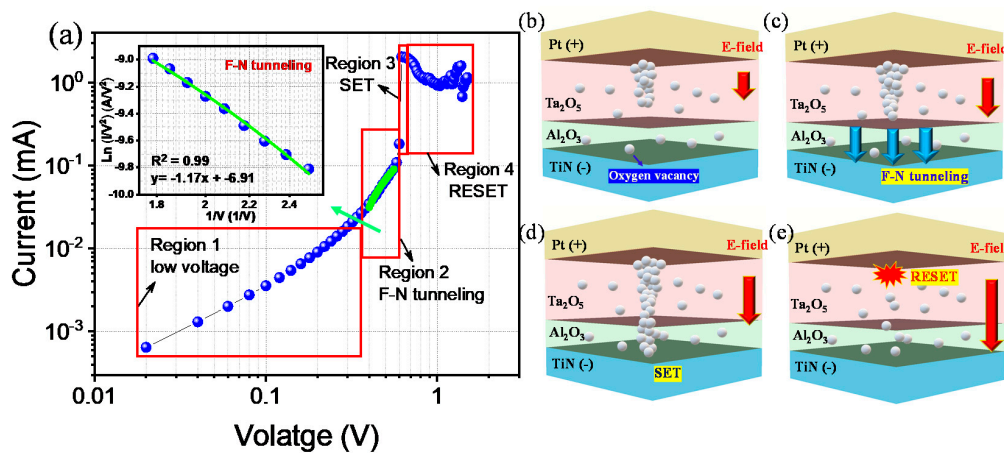


**Figure 6.** (a) Independent four regions of Pt/Ta<sub>2</sub>O<sub>5</sub>/Al<sub>2</sub>O<sub>3</sub> (3 nm)/TiN device by differentiating the conduction process. (Inset shows the fitting result of Fowler–Nordheim (F–N) tunneling to evaluate the linearity in the fitting region). Conducting path evolution of Pt/Ta<sub>2</sub>O<sub>5</sub>/Al<sub>2</sub>O<sub>3</sub> (3 nm)/TiN device in the positive bias. (b) high-resistance state (HRS); (c) FN tunneling in region 2; (d) LRS in region 3; (e) reset process in region 4.

#### 4. Conclusions

In summary, we proposed the intrinsic nonlinear characteristics in a Pt/Ta<sub>2</sub>O<sub>5</sub>/Al<sub>2</sub>O<sub>3</sub>/TiN RRAM device considering the Al<sub>2</sub>O<sub>3</sub> thickness effect. The optimized bilayer device (3-nm-thick-Al<sub>2</sub>O<sub>3</sub>) shows better nonlinearity. The improved read margin in Al<sub>2</sub>O<sub>3</sub> inserted devices are verified by the half-bias scheme simulation in cross-point structure. The XPS study verified the chemical state/element of the Ta<sub>2</sub>O<sub>5</sub>/Al<sub>2</sub>O<sub>3</sub>/TiN layer. The nonlinear properties are explained by the E-field-dependent conducting filament model process. This result can provide the feasibility of the selector-less RRAM approach in cross-point array structure.

**Supplementary Materials:** The following are available online at <http://www.mdpi.com/1996-1944/13/18/4201/s1>, Figure S1: Summary of the XPS working condition, Figure S2: Comparison of electroforming voltages, Figure S3: The simplified circuits for read margin in crossbar array structure.

**Author Contributions:** J.-H.R. conducted the electrical measurements and wrote the manuscript. S.K. designed the experiment concept and supervised the study. All authors have read and agreed to the published version of the manuscript.

**Funding:** This work was supported in part by a National Research Foundation of Korea (NRF) grant funded by the Korean government (MSIP) (2018R1C1B5046454) and by the Dongguk University Research Fund of 2020.

**Conflicts of Interest:** The authors declare that they have no competing interests.

#### References

- Frank, D.J.; Dennard, R.H.; Nowak, E.; Solomon, P.M.; Taur, Y.; Wong, H.S.P. Device scaling limits of Si MOSFETs and their application dependencies. *Proc. IEEE* **2001**, *89*, 259–287. [[CrossRef](#)]
- Wong, H.S.P.; Lee, H.Y.; Yu, S.; Chen, Y.S.; Wu, Y.; Chen, P.S.; Lee, B.; Chen, F.T.; Tsai, M.J. Metal-oxide RRAM. *Proc. IEEE* **2012**, *100*, 1951–1970. [[CrossRef](#)]
- Wong, H.S.P.; Raoux, S.; Kim, S.; Liang, J.; Reifenberg, J.P.; Rajendran, B.; Asheghi, M.; Goodson, K.E. Phase change memory. *Proc. IEEE* **2010**, *98*, 2201–2227. [[CrossRef](#)]
- Wu, H.; Wang, X.H.; Gao, B.; Deng, N.; Lu, Z.; Haukness, B.; Bronner, G.; Qian, H. Resistive Random Access Memory for Future Information Processing System. *Proc. IEEE* **2017**, *105*, 1770–1789. [[CrossRef](#)]
- Zheng, H.X.; Shih, C.C.; Chang, T.C.; Shih, L.Y.; Shih, Y.K.; Tseng, Y.T.; Chen, W.C.; Huang, W.C.; Yang, C.C.; Wu, P.Y.; et al. Indium Diffusion Behavior and Application in HfO<sub>2</sub>-Based Conductive Bridge Random Access Memory. *Phys. Status Solidi Rapid Res. Lett.* **2019**, *13*, 1900285. [[CrossRef](#)]

6. Zhou, J.; Cai, F.; Wang, Q.; Chen, B.; Gaba, S.; Lu, W.D. Very low-programming-current RRAM with self-rectifying characteristics. *IEEE Electron Device Lett.* **2016**, *37*, 404–407. [[CrossRef](#)]
7. Verdy, A.; d'Acapito, F.; Dory, J.B.; Navarro, G.; Bernard, M.; Noé, P. Effect of Nitrogen on the Amorphous Structure and Subthreshold Electrical Conduction of GeSeSb-Based Ovonic Threshold Switching Thin Films. *Phys. Status Solidi Rapid Res. Lett.* **2020**, *14*, 1900548. [[CrossRef](#)]
8. Ielmini, D.; Nardi, F.; Cagli, C.; Lacaita, A.L. Size-dependent retention time in NiO-based resistive-switching memories. *IEEE Electron Device Lett.* **2010**, *31*, 353–355. [[CrossRef](#)]
9. Lee, D.K.; Kim, G.H.; Sohn, H.; Yang, M.K. Ti-doped alumina based reliable resistive switching in sub- $\mu$ A regime. *Appl. Phys. Lett.* **2020**, *116*, 213503. [[CrossRef](#)]
10. Li, S.S.; Su, Y.K. Oxygen-Vacancy Induced Resistive Switching Effect in Mn-Doped ZnO Memory Devices. *Phys. Status Solidi Rapid Res. Lett.* **2019**, *13*, 1800453. [[CrossRef](#)]
11. Balatti, S.; Ambrogio, S.; Ielmini, D. Normally-off logic based on resistive switches—Part I: Logic gates. *IEEE Trans. Electron Devices* **2015**, *62*, 1831–1838. [[CrossRef](#)]
12. Kim, K.M.; Xu, N.; Shao, X.; Yoon, K.J.; Kim, H.J.; Williams, R.S.; Hwang, C.S. Single-Cell Stateful Logic Using a Dual-Bit Memristor. *Phys. Status Solidi Rapid Res. Lett.* **2019**, *13*, 1800629. [[CrossRef](#)]
13. Xu, N.; Fang, L.; Kim, K.M.; Hwang, C.S. Time-Efficient Stateful Dual-Bit-Memristor Logic. *Phys. Status Solidi Rapid Res. Lett.* **2019**, *13*, 1900033. [[CrossRef](#)]
14. Park, S.; Noh, J.; Choo, M.L.; Sheri, A.M.; Chang, M.; Kim, Y.B.; Kim, C.J.; Jeon, M.; Lee, B.G.; Lee, B.H.; et al. Nanoscale RRAM-based synaptic electronics: Toward a neuromorphic computing device. *Nanotechnology* **2013**, *24*, 384009. [[CrossRef](#)]
15. Zhang, W.; Gao, B.; Tang, J.; Li, X.; Wu, W.; Qian, H.; Wu, H. Analog-Type Resistive Switching Devices for Neuromorphic Computing. *Phys. Status Solidi Rapid Res. Lett.* **2019**, *13*, 1900204. [[CrossRef](#)]
16. Zhang, T.; Yang, K.; Xu, X.; Cai, Y.; Yang, Y.; Huang, R. Memristive Devices and Networks for Brain-Inspired Computing. *Phys. Status Solidi Rapid Res. Lett.* **2019**, *13*, 1900029. [[CrossRef](#)]
17. Luo, T.; Wang, X.; Qu, C.; Lee, M.K.F.; Tang, W.T.; Wong, W.F.; Goh, R.S.M. An FPGA-Based Hardware Emulator for Neuromorphic Chip with RRAM. *IEEE Trans. Comput. Des. Integr. Circuits Syst.* **2020**, *39*, 438–450. [[CrossRef](#)]
18. Wang, H.; Yan, X. Overview of Resistive Random Access Memory (RRAM): Materials, Filament Mechanisms, Performance Optimization, and Prospects. *Phys. Status Solidi Rapid Res. Lett.* **2019**, *13*, 1900073. [[CrossRef](#)]
19. Park, S.; Jung, S.; Siddik, M.; Jo, M.; Park, J.; Kim, S.; Lee, W.; Shin, J.; Lee, D.; Choi, G.; et al. Self-formed Schottky barrier induced selector-less RRAM for cross-point memory applications. *Phys. Status Solidi Rapid Res. Lett.* **2012**, *6*, 454–456. [[CrossRef](#)]
20. Chen, P.Y.; Yu, S. Compact Modeling of RRAM Devices and Its Applications in 1T1R and 1S1R Array Design. *IEEE Trans. Electron Devices* **2015**, *62*, 4022–4028. [[CrossRef](#)]
21. Gao, B.; Chen, B.; Liu, R.; Zhang, F.; Huang, P.; Liu, L.; Liu, X.; Kang, J.; Chen, H.Y.; Yu, S.; et al. 3-D cross-point array operation on  $\text{AlO}_x/\text{HfO}_x$ -based vertical resistive switching memory. *IEEE Trans. Electron Devices* **2014**, *61*, 1377–1381. [[CrossRef](#)]
22. Li, Z.; Chen, P.Y.; Xu, H.; Yu, S. Design of Ternary Neural Network with 3-D Vertical RRAM Array. *IEEE Trans. Electron Devices* **2017**, *64*, 2721–2727. [[CrossRef](#)]
23. Huang, Y.; Huang, R.; Pan, Y.; Zhang, L.; Cai, Y.; Yang, G.; Wang, Y. A new dynamic selector based on the bipolar rram for the crossbar array application. *IEEE Trans. Electron Devices* **2012**, *59*, 2277–2280. [[CrossRef](#)]
24. Li, Y.; Gong, Q.; Li, R.; Jiang, X. A new bipolar RRAM selector based on anti-parallel connected diodes for crossbar applications. *Nanotechnology* **2014**, *25*, 185201. [[CrossRef](#)]
25. Chen, Y.Y.; Goux, L.; Clima, S.; Govoreanu, B.; Degraeve, R.; Kar, G.S.; Fantini, A.; Groeseneken, G.; Wouters, D.J.; Jurczak, M. Endurance/retention trade-off on  $\text{HfO}_2$  metal cap 1T1R bipolar RRAM. *IEEE Trans. Electron Devices* **2013**, *60*, 1114–1121. [[CrossRef](#)]
26. Cheng, C.H.; Chou, K.I.; Zheng, Z.W.; Hsu, H.H. Low power resistive random access memory using interface-engineered dielectric stack of  $\text{SiO}_x/\text{a-Si}/\text{TiO}_y$  with 1D1R-like structure. *Curr. Appl. Phys.* **2014**, *14*, 139–143. [[CrossRef](#)]
27. Zhang, L.; Cosemans, S.; Wouters, D.J.; Groeseneken, G.; Jurczak, M.; Govoreanu, B. One-selector one-resistor cross-point array with threshold switching selector. *IEEE Trans. Electron Devices* **2015**, *62*, 3250–3257. [[CrossRef](#)]
28. Nardi, F.; Balatti, S.; Larentis, S.; Gilmer, D.C.; Ielmini, D. Complementary switching in oxide-based bipolar resistive-switching random memory. *IEEE Trans. Electron Devices* **2013**, *60*, 70–77. [[CrossRef](#)]

29. Kim, S.; Park, B.G. Nonlinear and multilevel resistive switching memory in Ni/Si<sub>3</sub>N<sub>4</sub>/Al<sub>2</sub>O<sub>3</sub>/TiN structures. *Appl. Phys. Lett.* **2016**, *108*, 212103. [[CrossRef](#)]
30. Choi, J.; Kim, S. Nonlinear Characteristics of Complementary Resistive Switching in HfAlO<sub>x</sub>-Based Memristor for High-Density Cross-Point Array Structure. *Coatings* **2020**, *10*, 765. [[CrossRef](#)]
31. Kim, S.; Jung, S.; Kim, M.H.; Cho, S.; Park, B.G. Resistive switching characteristics of Si<sub>3</sub>N<sub>4</sub>-based resistive-switching random-access memory cell with tunnel barrier for high density integration and low-power applications. *Appl. Phys. Lett.* **2015**, *106*, 212106. [[CrossRef](#)]
32. Chen, Y.C.; Lin, C.Y.; Huang, H.C.; Kim, S.; Fowler, B.; Chang, Y.F.; Wu, X.; Xu, G.; Chang, T.C.; Lee, J.C. Internal filament modulation in low-dielectric gap design for built-in selector-less resistive switching memory application. *J. Phys. D. Appl. Phys.* **2018**, *51*, 199501. [[CrossRef](#)]
33. Lee, Y.; Dumont, J.W.; George, S.M. Trimethylaluminum as the Metal Precursor for the Atomic Layer Etching of Al<sub>2</sub>O<sub>3</sub> Using Sequential, Self-Limiting Thermal Reactions. *Chem. Mater.* **2016**, *28*, 2994–3003. [[CrossRef](#)]
34. Egorov, K.V.; Lebedinskii, Y.Y.; Markeev, A.M.; Orlov, O.M. Full ALD Ta<sub>2</sub>O<sub>5</sub>-based stacks for resistive random access memory grown with in vacuo XPS monitoring. *Appl. Surf. Sci.* **2015**, *356*, 454–459. [[CrossRef](#)]
35. Hota, M.K.; Mahata, C.; Bera, M.K.; Mallik, S.; Sarkar, C.K.; Varma, S.; Maiti, C.K. Preparation and characterization of TaAlO<sub>x</sub> high-κ dielectric for metal-insulator-metal capacitor applications. *Thin Solid Films* **2010**, *519*, 423–429. [[CrossRef](#)]
36. Jiang, Y.; Shen, H.; Yang, W.; Zheng, C.; Tang, Q.; Yao, H.; Raza, A.; Li, Y.; Huang, C. Passivation properties of alumina for multicrystalline silicon nanostructure prepared by spin-coating method. *Appl. Phys. A Mater. Sci. Process.* **2018**, *124*. [[CrossRef](#)]
37. Siemensmeyer, B.; Bade, K.; Schultze, J.W. XPS and Electrochemical Studies of Thin TiN Layers. *Berichte der Bunsengesellschaft für Physikalische Chemie* **1991**, *95*, 1461–1469. [[CrossRef](#)]
38. Chand, U.; Huang, K.C.; Huang, C.Y.; Tseng, T.Y. Mechanism of Nonlinear Switching in HfO<sub>2</sub>-Based Crossbar RRAM With Inserting Large Bandgap Tunneling Barrier Layer. *IEEE Trans. Electron Devices* **2015**, *62*, 3665–3670. [[CrossRef](#)]
39. Kim, S.; Park, B.G. Tuning tunnel barrier in Si<sub>3</sub>N<sub>4</sub>-based resistive memory embedding SiO<sub>2</sub> for low-power and high-density cross-point array applications. *J. Alloys Compd.* **2016**, *663*, 256–261. [[CrossRef](#)]
40. Chen, Y.C.; Lin, C.Y.; Cho, H.; Kim, S.; Fowler, B.; Lee, J.C. Current-Sweep Operation on Nonlinear Selectorless RRAM for Multilevel Cell Applications. *J. Electron. Mater.* **2020**, *49*, 3499–3503. [[CrossRef](#)]
41. Chen, Y.-C.; Chang, Y.-F.; Lee, J.C. Selector-Less Graphite Memristor: Intrinsic Nonlinear Behavior with Gap Design Method for Array Applications. *ECS Trans.* **2018**, *85*, 11–19. [[CrossRef](#)]
42. Chen, Y.-C.; Lin, C.-C.; Kim, S.; Lee, J.C. Selectorless Oxide-Based Resistive Switching Memory with Nonuniform Dielectric for Low Power Crossbar Array Applications. *ECS Trans.* **2019**, *89*, 45–51. [[CrossRef](#)]
43. Kim, S.; Lin, C.Y.; Kim, M.H.; Kim, T.H.; Kim, H.; Chen, Y.C.; Chang, Y.F.; Park, B.G. Dual Functions of V/SiO<sub>x</sub>/AlO<sub>y</sub>/p<sup>++</sup>Si Device as Selector and Memory. *Nanoscale Res. Lett.* **2018**, *13*, 1–7. [[CrossRef](#)]
44. Yan, X.; Zhou, Z.; Ding, B.; Zhao, J.; Zhang, Y. Superior resistive switching memory and biological synapse properties based on a simple TiN/SiO<sub>2</sub>/p-Si tunneling junction structure. *J. Mater. Chem. C* **2017**, *5*, 2259–2267. [[CrossRef](#)]
45. Chakrabarti, S.; Samanta, S.; Maikap, S.; Rahaman, S.Z.; Cheng, H.M. Temperature-Dependent Non-linear Resistive Switching Characteristics and Mechanism Using a New W/WO<sub>3</sub>/WO<sub>x</sub>/W Structure. *Nanoscale Res. Lett.* **2016**, *11*, 389. [[CrossRef](#)] [[PubMed](#)]
46. Zhu, L.; Hu, W.; Gao, C.; Guo, Y. Parasitic resistive switching uncovered from complementary resistive switching in single active-layer oxide memory device. *Semicond. Sci. Technol.* **2017**, *32*, 125018. [[CrossRef](#)]
47. Chen, X.; Hu, W.; Li, Y.; Wu, S.; Bao, D. Complementary resistive switching behaviors evolved from bipolar TiN/HfO<sub>2</sub>/Pt device. *Appl. Phys. Lett.* **2016**, *108*, 053504. [[CrossRef](#)]
48. Tsai, T.M.; Chang, K.C.; Chang, T.C.; Zhang, R.; Wang, T.; Pan, C.H.; Chen, K.H.; Chen, H.M.; Chen, M.C.; Tseng, Y.T.; et al. Resistive switching mechanism of oxygen-rich indium tin oxide resistance random access memory. *IEEE Electron Device Lett.* **2016**, *37*, 408–411. [[CrossRef](#)]

